



This is a repository copy of *Elastic flow instabilities and macroscopic textures in graphene oxide lyotropic liquid crystals*.

White Rose Research Online URL for this paper:
<http://eprints.whiterose.ac.uk/170475/>

Version: Published Version

Article:

Wychowaniec, J.K., Iliut, M., Borek, B. et al. (4 more authors) (2021) Elastic flow instabilities and macroscopic textures in graphene oxide lyotropic liquid crystals. *npj 2D Materials and Applications*, 5 (1). 11.

<https://doi.org/10.1038/s41699-020-00193-x>

Reuse

This article is distributed under the terms of the Creative Commons Attribution (CC BY) licence. This licence allows you to distribute, remix, tweak, and build upon the work, even commercially, as long as you credit the authors for the original work. More information and the full terms of the licence here:
<https://creativecommons.org/licenses/>

Takedown

If you consider content in White Rose Research Online to be in breach of UK law, please notify us by emailing eprints@whiterose.ac.uk including the URL of the record and the reason for the withdrawal request.



eprints@whiterose.ac.uk
<https://eprints.whiterose.ac.uk/>

ARTICLE OPEN



Elastic flow instabilities and macroscopic textures in graphene oxide lyotropic liquid crystals

Jacek K. Wychowaniec^{1,2,3}, Maria Iliut², Bartłomiej Borek⁴, Christopher Muryń⁵, Oleksandr O. Mykhaylyk⁶, Steve Edmondson⁶ and Aravind Vijayaraghavan^{2,7}✉

Graphene oxide (GO) forms a well-aligned lyotropic liquid crystal (LC) phase in aqueous dispersions at relatively low concentrations. Under a remarkably wide range of shear rates, we report hitherto unobserved shear-induced polarized light image patterns, a Maltese cross combined with shear banding, recorded in real time and in situ during rheological measurements. This is shown to be a result of elastic flow instabilities that manifest as a helical flow in alternating bands of left- and right-handed helices, arising from a combination of shear flow and Taylor-type vortex flow. The instability is observed for LCs formed from large aspect ratio GO particles owing to their unique viscoelastic properties, but not for smaller aspect ratio particles. This phenomenon coincides with rheopecty and anomalous small-angle X-ray scattering patterns under shear flow, which confirm the instabilities. The results presented here could lead to advanced control over macroscopic periodic alignment in technologically relevant dispersions of two-dimensional material particles.

npj 2D Materials and Applications (2021)5:11 | <https://doi.org/10.1038/s41699-020-00193-x>

INTRODUCTION

Graphene and graphene oxide (GO) are being widely explored for applications including composites^{1–3}, electronics^{4,5}, ion-sieving membranes⁶, optical sensors⁷, and biomedical devices⁸. GO is known to form well-aligned layered liquid crystal (LC) structures in aqueous dispersions, above certain concentrations and particle sizes^{9–14}. For GO particles, simultaneously ordered states with liquid-like fluidity, as well as induced crystal ordering stem from intrinsic GO flake anisotropy^{15,16}. Such a system, known as a lyotropic phase, is typically charge- and sterically-stabilized¹⁷. It has also been shown that flow, confinement, and processing conditions affect the alignment and stability of these phases^{10,18–22}. The effect of flow on alignment has been previously reported for a variety of LCs^{23–26}. In particular, Cinader and Burghardt²³ developed a number of techniques for describing the alignment of LCs in the form of orientation parameters alongside orientation angles and corresponding orientation vectors. This made way for the rational design of LC molecules and corresponding methods of their alignment using shear, light, or chemical triggers^{11,27,28}. It is also known that phenomena such as Taylor vortices and similar elastic instabilities occur during shear flow of liquids^{29–31}. The formation of these instabilities may perturb, improve, or induce the alignment of the LC molecules present in the solvent³².

In the last decade, increasing attention has been paid to the processing and applications of two-dimensional (2D) materials. In particular, GO is processed using electro-spinning, wet spinning, inkjet printing, injection molding, or microfluidics etc.^{19,33–35} to form graphene fibers, composites, and printed electronics. In all of these processes, graphene-based dispersions in various media are subject to high shear. Naficy et al.³⁶ discuss the viscoelastic properties of GO dispersions, using as model ultra-large GO sheets with a high aspect ratio (45,000) to study the LC phase transitions from isotropic to nematic. They show the typical shear-thinning

behavior of GO flakes and link the viscosity to both the LC phase composition and the concentration. This serves as a motivation to monitor rheological properties of GO dispersions with polarized light image (PLI) to allow direct LC phase observation in situ. One method that combines rotational rheology and optical birefringence-based techniques and allows full view of a sample during rheological measurements using various geometries and different states of polarized light has been developed called shear-induced polarized light imaging (SIPLI)^{27,37,38}.

In this work, we report on the alignment of monolayer GO flakes of two lateral sizes (large: GO-L and small: GO-S) in liquid crystalline suspensions under a wide range of shear flow conditions. We observe and image the exact orientation of GO flakes in situ and in real time using SIPLI (Fig. 1) and small-angle X-ray scattering (SAXS), both coupled with mechanical rheometers (referred to henceforth as Rheo-SIPLI and Rheo-SAXS, respectively). Prior to shear, all GO dispersions showed conventional lyotropic or isotropic phases. Under certain GO particle size, concentration, and shear rate conditions, we observed unique patterns in Rheo-SIPLI, indicating shear banding (SB) producing a stable, periodic, and macroscopic alignment of GO flakes. This phenomenon coincides with rheopecty and anomalous Rheo-SAXS patterns. Our analysis and model points to the onset of Taylor-vortex type flow instigated by elastic instabilities that occur in the flow, resulting in alternating bands of left-hand and right-handed helical flows. It is likely that this unique flow is a result of the viscoelastic properties of graphene oxide liquid crystals (GOLC).

RESULTS AND DISCUSSION

Anomalous patterns observed in Rheo-SIPLI of GOLCs

Previous reports concerning rheological behavior and alignment of GO in suspensions typically involved flakes of lateral sizes no

¹Manchester Institute of Biotechnology, The University of Manchester, Manchester M13 9PL, UK. ²Department of Materials, The University of Manchester, Manchester M13 9PL, UK. ³School of Chemistry, University College Dublin, Belfield, Dublin 4, Dublin, Ireland. ⁴RHL-SERVICE, ul. Budziszewska 74, 60-179, Poznań, Poland. ⁵Department of Chemistry and Photon Science Institute, The University of Manchester, Manchester M13 9PL, UK. ⁶Soft Matter Analytical Laboratory, Department of Chemistry, The University of Sheffield, Sheffield S3 7HF, UK. ⁷National Graphene Institute, The University of Manchester, Manchester M13 9PL, UK. ✉email: aravind@manchester.ac.uk

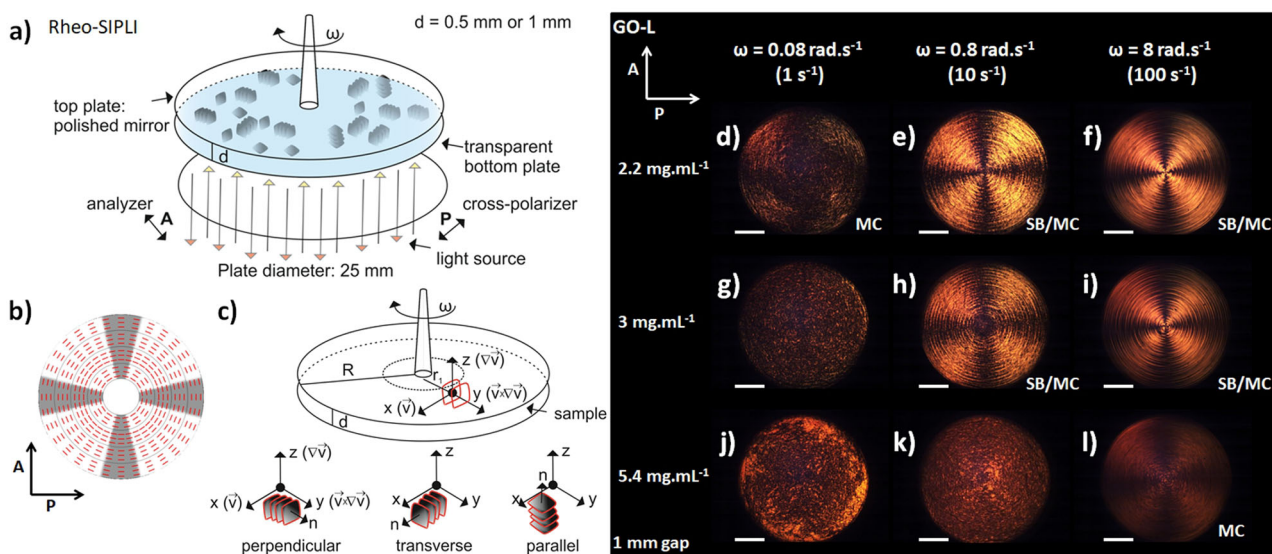


Fig. 1 GOLCs alignment phase state diagram using Rheo-SIPLI. **a** Schematic representation of the parallel-plate shear geometry used for Rheo-SIPLI. The diameter of the top plate used was kept at 25 mm. The double-sided arrows show plane of polarization of the polarizer (P) and the analyzer (A) perpendicular to each other. The angular speed (ω) indicates the axis and direction of rotation of the top shear plate. **b** A schematic representation of GO flake alignment directions in the parallel-plate geometry (top-view) with a corresponding Maltese Cross pattern which could be observed for this alignment in polarized light images, the arrows show plane of polarization of P and A. **c** Possible GO flake orientations in the parallel-plate shear geometry used for Rheo-SIPLI (parallel, perpendicular, and transverse) schematically depicted with respect to the shearing directions. In the cylindrical coordinate system employed here, x, y, and z correspond to flow, vorticity, and shear gradient direction, respectively. The GO flake orientation is denoted by the normal vector to the flake surface. **d–l** SIPLIs of GO-L dispersion at three concentrations (indicated by the left column) using different angular speed of rotation (indicated by the top line, shear rates produced at the sample edge are shown in brackets), captured at the end of a 120 s shear pulse. The shearing plates were set at 1 mm gap. SB and MC indicate that apparent vorticity shear banding (SB) and/or Maltese Cross (MC) is observed. The diameter of the polarized light images is 25 mm (corresponding to the diameter of the top plate). Scale bar on SIPLIs depicts 5.86 mm.

greater than $20\ \mu\text{m}$ ^{18,39} that in parallel-plate geometry exhibit shear-thinning and align parallel to the flow direction and perpendicular to the shearing plates^{14,18,36} (alignment shown schematically in Fig. 1b, c). The coordinate system employed in our work is cylindrical, with x and y corresponding to tangential and radial directions, respectively. In the parallel-plate SIPLI configuration, shear flow in the tangential direction (tracing a circular trajectory around the rheometer axis of rotation)^{27,38} should align GO flakes so as to produce a PLI illustrated in Fig. 1b (for discussion on employed geometry see Methods).

Recently, improved exfoliation techniques have allowed the production of ultra-large GO flakes for various applications, such as filtration membranes or printed electronics^{19,33,34}. Here, we therefore first consider large GO flakes (GO-L) with typical log-normal size distribution of $42.1 \pm 29.4\ \mu\text{m}$ (a full characterization of the flakes is included in Supplementary Figs. 1 and 2). The typical range of aspect ratios for our GO-L flakes is 12,700–71,500 with an average value of $\sim 42,100$, comparable to GO flakes produced by Naficy et al.³⁶, but larger than typically used flakes^{14,18,40}. Using Onsagers theory^{18,41}

$$\phi_c \approx \frac{4t}{D} \quad (1)$$

where t is the flake thickness and D is the diameter, we estimate the empirical value of the critical volume fraction corresponding to isotropic to nematic LC transition of our GO-L flakes to be $\phi_c \approx 1 \times 10^{-4}$ (corresponding to $\sim 0.1\ \text{mg mL}^{-1}$).

First, Rheo-SIPLI was used to study birefringence of aqueous dispersions of GO-L flakes at three different concentrations, all an order of magnitude larger than the predicted ϕ_c , ensuring that we are in the full nematic phase¹⁴, as a function of shear rate (Fig. 1d–l). In this experiment, angular speed was increased from $\omega = 0.08\ \text{rad s}^{-1}$ (Fig. 1d, g, j) to $\omega = 0.8\ \text{rad s}^{-1}$ (Fig. 1e, h, k) and finally

$\omega = 8\ \text{rad s}^{-1}$ (Fig. 1f, i, l). PLIs were recorded during a shearing time of 120 s, as well as before and after the shear pulse.

All samples were also imaged under quiescent conditions prior to a shear pulse ($\omega = 0\ \text{rad s}^{-1}$) and displayed typical PLIs with bright and dark regions corresponding to randomly oriented lyotropic domains^{12,13} (Supplementary Figs 3a–c). The PLI pattern changes with the change of angular speed (Fig. 1d–l). Initially, for $2.2\ \text{mg mL}^{-1}$ GO-L dispersion, the pattern clearly showed a Maltese Cross (MC) at shear rates above $1\ \text{s}^{-1}$ (Fig. 1d), with a randomly patterned central region (truncated MC) below this threshold value. Subsequently, the higher the angular speed, the more pronounced is the observed MC (Fig. 1e and f) with the radius of the central region of the truncated MC becoming smaller, similar to what has been observed for polymer melts³⁷.

At the higher shear rates, striking and very well-defined SB, i.e., circular streaks alternating along the vorticity direction, superimposed on the MC, were observed for both the $2.2\ \text{mg mL}^{-1}$ GO-L (Fig. 1e, f) and the $3\ \text{mg mL}^{-1}$ GO-L (Fig. 1h, i). At the highest concentration of $5.4\ \text{mg mL}^{-1}$ and low angular speeds, neither SB nor MC was observed. Only at the highest angular speed of $\omega = 8\ \text{rad s}^{-1}$ the MC was observed, but still no SB (Fig. 1l). This suggests that there is an upper bound of concentration for a given GO flake size distribution, where the SB can no longer be observed owing to the onset of turbulent flow. Furthermore, it is likely that there is also an upper bound of shear rate for lower concentrations, at which the banding will disappear owing to the onset of turbulent flow. However, owing to the geometrical constraints of our Rheo-SIPLI system, where the dispersion is held between two shear plates without any circumferential boundary, any higher shear rate will result in the centrifugal ejection of the dispersion, limiting investigations at higher shear rates. We chose $3\ \text{mg mL}^{-1}$ concentration for the further investigation, as it produces the most pronounced PLI banding that is retained at $\omega = 8\ \text{rad s}^{-1}$. At first glance, this could

be interpreted as vorticity banding (i.e., with bands stacked in the global vorticity direction imposed by the shear), as the observed combination of MC and SB appears similar to the radially stacked bands seen in PLIs of the well-known banded spherulites⁴². Detailed consideration of banded spherulites and related structures has been helpful in interpreting our PLIs. However, a fundamentally different explanation is required here, as we have rapidly flowing liquid system rather than static crystalline (or liquid crystalline) material. Therefore, we refer to the observed structure as “apparent vorticity SB” leading up to the elucidation of the underlying mechanism in subsequent paragraphs.

In a previous report, gradient SB (i.e., with bands stacked in the velocity gradient direction) was observed in the Couette concentric cylinder geometry for aqueous GO dispersions⁴³, with no associated imaging reported. The proposed jamming mechanism produces gradient shear bands parallel to the sheared surface, inconsistent with our findings. To our knowledge, there are very few further examples of concentric bands in parallel-plate geometry such as ours, with bands only observed over a narrow shear rate range and/or only for carefully selected fluids^{30,31,44,45}. In one example by Rennie and co-workers, a dispersion of inorganic discs of nickel hydroxide with a diameter of about 80 nm and a thickness of 8 nm in a columnar phase was studied using a range of shear rates⁴⁴. It has to be noted that the aspect ratio of these discs is orders of magnitude less than our GO flakes and, therefore we do not expect the details of the mechanism to be applicable to our case. In addition, we do not believe that the proposed tilted structure can generate an offset MC under cross polarizers as we observed.

Kang et al.⁴⁶ have studied apparent vorticity banding in dextran-containing suspensions of semi-flexible colloidal phase fd virus rods of aspect ratio ~ 133 . In a Couette shear cell these particles exhibited bands under cross-polarized light of different orientational order, stacked along the vorticity direction. The authors concluded that this non-equilibrium phenomenon arises in biphasic isotropic-nematic regions owing to elastic deformation of inhomogeneity formed during phase separation, with formation reported to take an hour. Unlike phage fd rod-like virus particles, our significantly higher aspect ratio GO-L formed bands instantaneously in the parallel-plate arrangement (Supplementary Video 1) and also appear to be stacked along the vorticity direction. However, our concentrations used are much greater than the biphasic isotropic-nematic region suggesting that the separation of phases is not the mechanism that triggers our vorticity band formation. Recently Hong et al.⁴⁷ have published findings on GO dispersions in a coaxial cylinder shearing cell, which at first appear to be consistent with our observations. However, detailed analysis reveals different flow-regime type stemming from internal differences in materials composition and concentration, with no vorticity banding observed by Hong et al. under cross-polarized microscopy and minimal explanation for the phenomena provided with no correlation to rheological parameters attempted. Furthermore, the effects observed by Hong et al. appear to only arise due to surface-effects, whereas our observed banding remains conserved throughout the thickness (gap) of the cells (1 mm).

Our observed bands in sheared GO-L dispersions are extremely stable (spatially and temporally, see Supplementary Video 1: Rheo-SIPLI of GO-L 3 mg mL⁻¹, a time-lapse showing 120 s of shear followed by 60 s at quiescent conditions after the shear stops), very well-defined and form over a very wide range of shear rates (0.5–100 s⁻¹). To better visualize and analyze the complex patterns, we performed a polar to Cartesian coordinate transformation of the SIPLI images, shown in Fig. 2 for the 3 mg mL⁻¹ GO-L sample processed at $\omega = 8$ rad s⁻¹ (edge shear rate of 100 s⁻¹). Two lines in Fig. 2b represent directions (R₀—tangential and R—radial) along which two different features can be observed: MC and SB, respectively. In order to remove the MC (representing

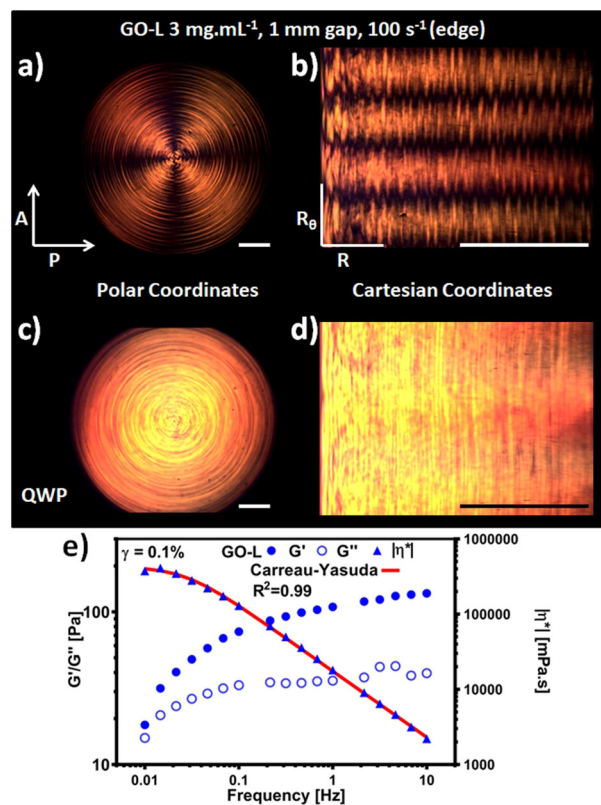


Fig. 2 PLIs and oscillatory rheology of 3 mg mL⁻¹ GO-L. PLIs of 3 mg mL⁻¹ GO-L obtained during a shear pulse using angular speed $\omega = 8$ rad s⁻¹ (sample edge shear rate is 100 s⁻¹). **a** Using linearly polarized light and represented in polar coordinates as recorded, arrows labeled by P and A define polarization plane orientations of polarizer and analyzer, respectively, and **b** a corresponding transformed image represented in Cartesian coordinates. The two-line plots R₀—tangential and R—radial show directions at which two different features can be observed: Maltese cross in the R₀ direction and apparent vorticity shear bands in the R direction. **c** Using circularly polarized light produced by quarter wave plates (QWP) and represented in polar coordinates, and **d** a corresponding transformed image represented in Cartesian coordinates. Diameter of the PLI is 25 mm (corresponding to the diameter of the top plate). **e** Frequency sweep of GO-L performed using parallel-plate geometry in oscillatory mode (disc diameter 60 mm and a gap $d = 0.5$ mm). Red line represents the Carreau-Yasuda-model fitting using Eq. (2). Scale bar on SIPLIs depicts 5.86 mm.

isogyres) and isolate the SB, Rheo-SIPLI was repeated on GO-L using a circularly polarized light produced by quarter wave plates (QWPs) incorporated in the optical path (Fig. 2c). In this setup, only circles of apparent vorticity shear bands corresponding to lines of constant birefringence (usually called isochromatic or isostress lines)⁴⁸ are observed. The circularly PLIs (Fig. 2d), reveal the fact that the bands are continuous and virtually concentric around the axis of rotation. This observation, combined with a closer inspection of the polar and Cartesian representations of the linearly polarized PLI (Fig. 2a, b) reveals that in fact, the pattern consists of concentric bands, each containing a frustum of the MC alternately offset in opposite tangential directions.

The onset of instabilities fits with theory

A frequency sweep on GO-L (Fig. 2e), performed at a strain within the linear viscoelastic region ($\gamma = 0.1\%$), revealed that the 3 mg mL⁻¹ GO-L dispersion exhibited different rheological behavior to that of Naficy et al.³⁶. The $G' = G''$ point in our case occurs at very

low frequencies (~ 0.01 Hz), indicating that the time scale of relaxation of the GO flakes is of the order of seconds or more. By applying the Carreau-Yasuda model^{49,50}, described by the following equation:

$$\eta = \eta_{\infty} + \frac{(\eta_0 - \eta_{\infty})}{(1 + (\lambda\Omega)^a)^{\frac{1-a}{a}}} \quad (2)$$

(where Ω defines the angular frequency, η and η_{∞} define viscosities at a given point and at infinity, respectively, and parameter a set to 2, typical for carbon LC systems⁵⁰) to the modulus of complex viscosity data obtained from GO-L frequency sweeps (Fig. 2e), the relaxation time of the studied system (λ) can be calculated as 5.48 ± 0.90 s. In this respect the Deborah number (De) can be used to estimate critical conditions (De_{crit}) for a development of elastic flow instabilities in viscoelastic fluids sheared by cone-plate or parallel-plate geometries³⁰. De , used in rheology to describe the character of the material under specific flow conditions, is defined for cone-plate or parallel-plate geometries as:

$$De = \lambda\omega \quad (3)$$

where ω is the angular speed of the upper cone or disc plate³⁰. Using the extracted relaxation time and the rotational speeds of the SIPLI experiments, De could be calculated as 0.44, 4.39, and 43.87 for 0.08, 0.8, and 8 rad s^{-1} , respectively (Supplementary Table 1). Calculated and measured values for De_{crit} vary and depend on fluid properties and experimental geometry, but are typically between 1 and 8 ($1 < De_{crit} < 8$)^{30,51,52}. The De_{crit} values obtained for GO-L matches well with these predictions, where at the lowest rotational speed (0.08 rad s^{-1} , $De = 0.44$) the flow remains stable, whereas at higher rotational speeds ($De = 4.39$ or 43.87) it becomes unstable producing the MC + SB pattern (Figs 1 and 2). Thus, De_{crit} for the studied system should be about 4.39 or below.

Close inspection of the SIPLI image taken after 120 s of constant shear at $\omega = 0.08 \text{ rad s}^{-1}$ with sample edge (maximum) shear rate of 1 s^{-1} (Fig. 1e) reveals that the apparent vorticity bands are about to form at the sample edge. However, the next image (Fig. 1g) taken after 120 s of constant shear at $\omega = 0.8 \text{ rad s}^{-1}$ (with edge shear rate of 10 s^{-1}) shows a clear distinction between the middle non-banded region and the outer banded region. Using this image (Fig. 1g) and Eq. (4) (see Methods) we can estimate that the critical shear rate necessary to induce apparent vorticity bands in this experiment is $\sim 1 \text{ s}^{-1}$, considering the fact that in parallel-plate geometry the shear rate is radially increasing. Thus, the Weissenberg number associated with the observed instabilities (Fig. 1g) is ~ 5.48 ($Wi_{crit} = \lambda\dot{\gamma} = 5.48 \text{ s} \times 1 \text{ s}^{-1}$, Supplementary Table 1) or higher, considering the fact that the observed instabilities are well established at shear rates above 3 s^{-1} . The obtained critical Weissenberg number ($Wi_{crit} = 5.48$) together with $De_{crit} = 4.39$ estimated for this experiment (Supplementary Table 1) seems to be consistent with the instability predictions presented in Shaqfeh's review³⁰.

Flow modeling suggests vorticity-driven Taylor-like rolls

As noted by Jin et al.⁵³, there are three identified types of instabilities that lead to banded states, which are commonly referred to as: (1) gradient-banding, (2) vorticity banding, and (3) shear-gradient concentration coupling instability. Considering only shear flow, it is possible to predict the observed MC from SIPLI (Fig. 1b). However, to explain the apparent vorticity SB we propose that Taylor-like vortices are also formed⁵⁴. Such vortices are more commonly encountered at high shear rates in the Taylor-Couette concentric cylinder geometry^{28,29} but have also been reported in parallel-plate geometry^{29,30}. Counter-intuitively, the axes of these vortices are known to be tangential, i.e., parallel to the flow direction, around the circle. As also noted by Jin et al. the

kinetics of shear-banding formation, as well as the final state of banded structures, depend on the shear-gradients that are naturally present in the experimental shearing geometry⁵³, in our initial case: parallel-plate geometry.

To represent and analyze the flow and flake alignment leading to these unique MC + SB patterns, we propose a model consisting of a linear combination of shear and vortex flow with flake normals in the vorticity direction (Fig. 3 and Supplementary Fig. 4). Full details can be found in the Supplementary Discussion. The observed MC + SB patterns are superficially similar to those observed under crossed polarizers for banded spherulites due to periodically twisted lamellae⁴², or the "spiral stripes" possible with cholesteric LCs²⁸. In these cases, the concentric bands are due to helical changes in alignment, but crucially the helix axis is in the radial direction, rather than in the tangential direction as for the vortex axis in our proposed Taylor-like rolls of elastic instability-driven alignment. For 2D flakes such as GO-L, radial helices would either produce no bands at all (if the flakes are aligned in the perpendicular direction) or produce darker and lighter bands as the flakes alternate between parallel and transverse orientations; no such dark bands are observed. We believe the offset banded MC pattern is completely and uniquely explained by the presence of Taylor-like vortices in which the flakes are aligned with the surface normal in the vorticity direction (as for the perpendicular alignment in the non-vortex case).

Confirmation of predicted flake alignment using Rheo-SAXS

To confirm the proposed helical vortex flow and explain the orientation of GO flakes and the abrupt changes between bands, Rheo-SAXS in the coaxial cylinder geometry (Fig. 4a) was used as an alternative method of analysis. The arrangement comprises two concentric cylinders, a fixed outer cylinder and a rotating inner cylinder, providing the two shear surfaces between which fluid is confined. X-rays impinge on the cylinders laterally, perpendicular to the cylinder walls. The Cartesian coordinate system employed here is matched to the Cartesian coordinates from the SIPLI parallel-plate setup, such that the axes corresponding to the direction of flow and the normal to the shearing planes remain the same in both cases, allowing consistent comparison. The scattering can be measured at two different positions: radial or tangential.

This is a significant difference to the relationship between the light rays and the shear flow in SIPLI, where light is always passing through the sample along the z axis. In Rheo-SAXS, the X-ray beam passes through the sample along the z axis in the radial position but along the x axis in the tangential position. It was already shown that the scattering intensity of GO at the radial position is 100-fold lower than that of the tangential geometry¹⁸, yet it provides required information about the sheared sample that can be directly correlated to the PLIs obtained in the parallel-plate geometry.

Hence, 2D scattering patterns were recorded during shear in the radial geometry and the tilt angle of the overall anisotropic scattering ($\Phi = 0 \rightarrow 2\pi$) was calculated using procedures developed by Cinader and Burghardt⁵⁵ in which an orientation angle and orientation parameter are derived from a weighted average of the second moment tensor of the scattering pattern (from the eigenvectors and difference in eigenvalues, respectively). This analysis shows that for GO-L flakes, the orientation angle (tilt angle) throughout 1000 s of shear measurement varied but indicated a tilt in the x - y plane (Fig. 4b). The calculated tilt angle (Φ) was typically between 75° and 80° . This indicated that angle between the GO flake plane and flow direction (Θ) was between 15° and 10° , of a similar magnitude to the offset of the MCs (12.5°) observed in Rheo-SIPLI (Supplementary Fig. 5). Throughout the measurement, the tilt angle was changing. At the beginning of the measurements, the tilt angle was lowest (45°), whereas at 420 s

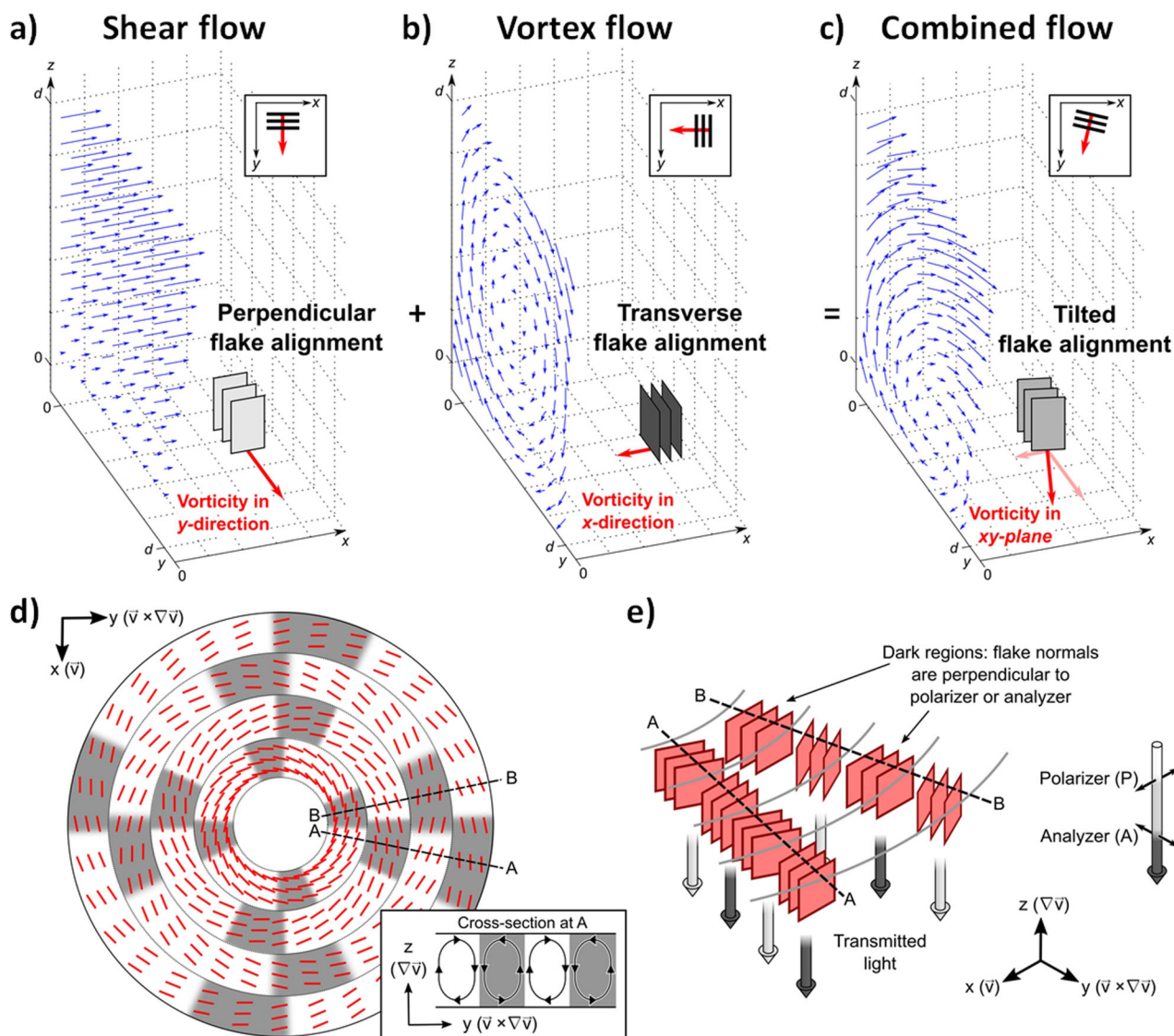


Fig. 3 Mathematical vector field model. Mathematical vector field model was developed to describe the behavior of GO flakes under **a** shear flow, **b** vortex flow and **c** combined shear and vortex flows. Upon combination of the two fields, the combined field is helical and produces vorticity in the x - y plane (Fig. 1c). **d** Top-view flake alignment depicting flakes aligned with their normal vector in the vorticity direction under combined flow. The presented pattern is the outcome of the mathematical flow fitting and matches well with the offset Maltese cross and banding observed in the polarized light image. Inset: cross-section at line A showing the counter-rotating vortex flows responsible for the flake tilts **e** Isometric 3D depiction of the cross-sections at lines A and B in part d, demonstrating how dark regions result from flakes aligned with their normals perpendicular to the polarizer or analyzer direction. The z -scale of the proposed vortices has been compressed for clarity, and flake dimensions are not representative.

the tilt angle was highest (90°). This result indicated that GO flakes were undergoing dynamical, abrupt changes, in which they were experiencing forces from combined shear and vortex flow. If there were no vortices or very weak vortices present, the tilt angle would quickly stabilize at 90° throughout the measurement (as drawn in Fig. 4a—the perpendicular orientation shown in Fig. 1c). The dynamical changes were also observed during Rheo-SIPLI recording (Supplementary Video 1: Rheo-SIPLI of GO-L 3 mg mL^{-1}), where the radial position of the bands fluctuates within one radial pitch. The dynamics of the vorticity banding reported by Kang et al.⁴⁶ appear to be very similar to our case, with bands moving dynamically in the vorticity direction. Interestingly, the observed dynamics and the Taylor-like apparent vorticity bands show similar behavior to the platelet system studied by Lettinga et al.⁵⁶ during large amplitude oscillatory shear flow-SAXS in a Taylor-Couette cell. Overall, the abrupt changes observed in both

techniques support the formation of Taylor vortices and Taylor-like rolls.

It is predicted that during the formation of instabilities, such as Taylor vortices^{45,46}, in high shear flow of various dispersions, additional forces are generated perpendicular to the flow direction. Such vortex formation would lead to an increase in the apparent viscosity and appear as rheopecty, where the viscosity of dispersion increases with time⁵⁷. Indeed, the expected rheopecty behavior due to the formation of Taylor vortices was observed for the whole duration of the GO-L Rheo-SIPLI measurement, with the highest viscosity increase in the first 10 s of the measurement (Fig. 4c). This rapid change was accompanied by a change in the SIPLI pattern, as shown in the Fig. 4d. For 3 mg mL^{-1} GO-L, it took $<10 \text{ s}$ to form fully coherent banding across the whole sample, from highest shear rate (100 s^{-1} , edge) to the lowest (0 s^{-1} , center). Note that the rheopecty (14.2% viscosity

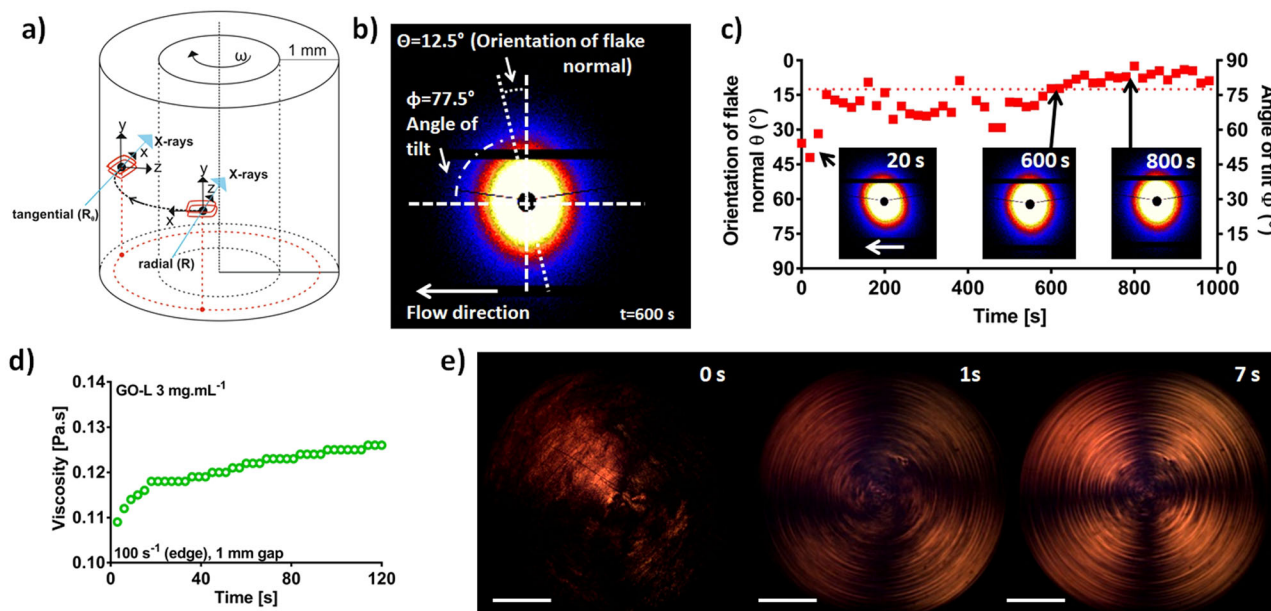


Fig. 4 Rheo-SAXS of 3 mg ml⁻¹ GO-L. **a** A coaxial cylinder shearing cell in Rheo-SAXS measurements with two probed locations in the cell depicted: Radial (R) and Tangential (R_θ). The Cartesian coordinate system associated with the dispersion flow (x, y, and z corresponds to flow, vorticity and shear gradient direction, respectively, see also Fig. 1c) was mapped onto the coaxial cylinder cell, where the arrowed black dotted line reproduces a trace of flow and a movement of the Cartesian coordinates. **b** 2D SAXS pattern obtained at 600 s time point, illustrating the relationship between the conventional tilt angle of SAXS pattern (Φ) and orientation of the flake normal (Θ). Direction of shear is depicted by the white arrow. **c** Orientation angle of 3 mg ml⁻¹ GO-L sheared in coaxial cylinder geometry at $\omega = 4.17 \text{ rad s}^{-1}$ (shear rate of 100 s^{-1}) with a 1 mm gap, in the radial direction, as a function of time taken during the shear experiment. Dashed line shows alignment of 12.5°, which corresponds to the observed offset between the MCs in the Rheo-SIPLI. The representative 2D SAXS patterns of sheared GO-L corresponding to three different time points (three different frames) show evolution of scattering pattern. Direction of shear is depicted by the white arrow. **d** Time sweep parallel-plate rheology of GO-L at 3 mg ml⁻¹ ($\omega = 8 \text{ rad s}^{-1}$, edge shear rate of 100 s^{-1}), rheopecty is observed during the course of the measurement. **e** Representative SIPLI data showing the evolution of patterns during vortex formation for the first 7 s of measurements. Scale bar on SIPLIs depicts 5.86 mm.

increase over 120 s) in our case is expected to be small, compared with the large shear-thinning behavior typically observed in GOLCs⁴⁰. The evolution of the pattern in time can be seen in the Supporting Information (Supplementary Video 1: Rheo-SIPLI of GO-L 3 mg ml⁻¹).

Different behavior with smaller GO flakes

We repeated our SIPLI and rheology investigation on GO with significantly lower lateral size (GO-S) of $15.5 \pm 7.5 \mu\text{m}$, with the corresponding range of aspect ratios 8000–23,000 with an average value of $\sim 15,500$, comparable to typical flakes reported in literature^{14,18,40}. The critical volume fraction for the nematic LC transition for GO-S is predicted to be approximately three times higher ($\phi_c \approx 3 \times 10^{-4} \sim 0.3 \text{ mg mL}^{-1}$) than for GO-L flakes. Likewise, GO-S at 3 mg ml⁻¹ was also imaged under quiescent conditions prior to a shear pulse ($\omega = 0 \text{ rad s}^{-1}$) and displayed typical PLIs with bright and dark regions corresponding to randomly oriented lyotropic domains (Fig. S3c). SIPLI data of 3 mg ml⁻¹ GO-S at angular speed of $\omega = 8 \text{ rad s}^{-1}$ (full evolution of the pattern in time can be seen in Supplementary Video 2: Rheo-SIPLI of GO-S 3 mg ml⁻¹) clearly show the MC pattern (Fig. 5). Closer inspections of the image (Fig. 5a) may suggest Taylor-like rolls similar to GO-L. However, after the image is transformed using the same procedure as for GO-L, a smeared pattern was obtained in Cartesian coordinates (Fig. 5b). It was not possible to trace a single band along any vertical (tangential) line (R_θ) on this image. This smeared phase suggested the lack of formation of Taylor vortices. The same conclusion has been made using circularly polarized light (QWP image) (Fig. 5c). Although at first, it may seem that there are clear shear bands present, the transformed Cartesian QWP image (Fig. 5d) showed only a smeared phase with no

possibility of tracing a single band across an image (R_θ direction) either, further supported by a comparison of Fourier transforms of QWP images (Supplementary Fig. 6). This suggests that only flakes of sufficient lateral size will result in vortexing and show Taylor-like roll phenomena.

To confirm the SIPLI observations, the Rheo-SAXS experiments in coaxial geometry were repeated for GO-S (Fig. 5e). In particular, very strong anisotropic patterns from GO-S in the radial direction indicated that the flakes were aligned along the direction of flow (perpendicular alignment). Analysis of the angle of tilt not only confirmed the perpendicular alignment observed in the 2D scattering patterns (constant $\Phi = 90^\circ$ angle of tilt throughout the time of measurement), but also showed no dynamical changes of structure during whole duration of shear. It is worth noting that this obtained alignment for GO-S corresponds to the same anomalous patterns observed by Poulin et al.¹⁸ for a similar GO flake size distribution to our GO-S. Overall, these results suggest generation of significantly weaker vortices by the GO-S flakes during shear and point toward the importance of lateral size for the formation of Taylor vortices driven alignment. As expected, the rheological behavior of GO-S varied significantly from GO-L. Indeed, as shown in Fig. 5f, there was no rheopecty observed for GO-S flakes (only an insignificant viscosity increase of $\sim 1.5\%$ was detected, Fig. 5f) when sheared under the same conditions as GO-L (14.2% viscosity increase, Fig. 4c). The relaxation time of GO-S flakes, as extracted from the Carreau-Yasuda model fitted to the frequency sweeps (Fig. 5g) was calculated as $\lambda = 9.57 \pm 0.97 \text{ s}$, which is of a similar order to that of GO-L. The *De* numbers 0.77, 7.65, and 76.52 were obtained for SIPLI rotational speeds 0.08, 0.8, and 8 rad s⁻¹, respectively (Supplementary Table 1). Consequently, these numbers suggest that at low shear rates the GO-S flow should remain stable ($De < De_{crit}$), whereas at larger shear rates

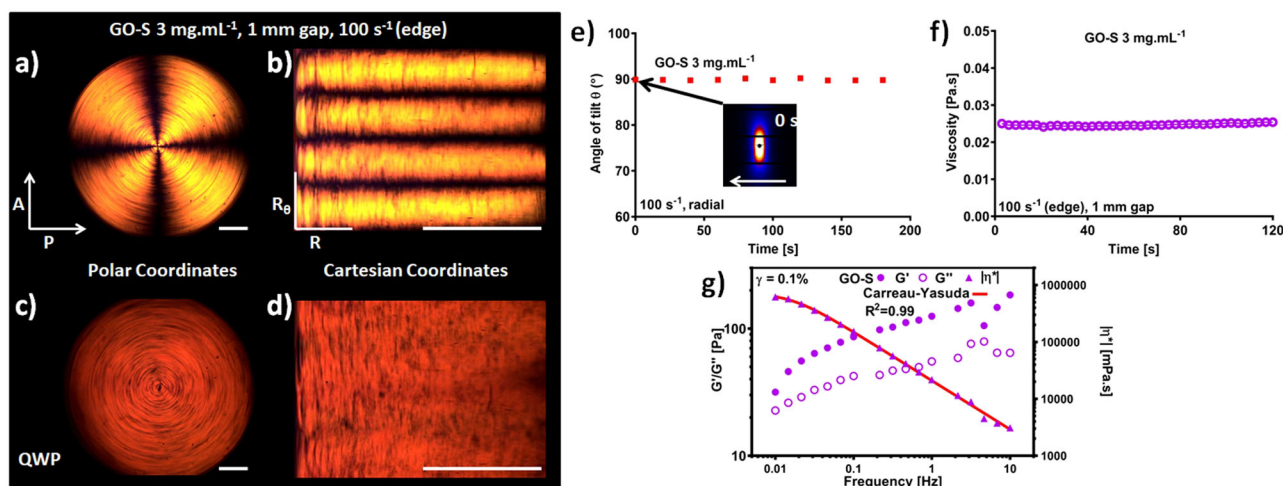


Fig. 5 Different behavior with smaller GO flakes. **a** PLI of GO-S, as obtained, in polar coordinates. Diameter of the polarized light image is 25 mm. P and A define directions of polarizer and analyzer plane. **b** Transformed image of GO-S in Cartesian coordinate system. The two-line plots R_θ —tangential and R—radial show directions at which two different features could be observed: Maltese cross in the R_θ direction and apparent vorticity shear bands in the R direction. **c** Quarter wave plate (QWP) SIPLI of 3 mg mL⁻¹ GO-S with the shear rate at the edge of 100 s⁻¹. **d** Transformed QWP image of GO-S in Cartesian coordinates. Scale bar on SIPLIs depicts 5.86 mm. **e** Orientation angle of 3 mg mL⁻¹ GO-S sheared in coaxial cylinder geometry at $\omega = 4.17$ rad s⁻¹ with a 1 mm gap, in the radial direction, as a function of time taken during the shear experiment. Initial 2D SAXS pattern obtained for GO-S is embedded in the graph. Direction of shear is depicted on the 2D pattern by the white arrow. **f** Time sweep parallel-plate rheology of GO-S at 3 mg mL⁻¹ ($\omega = 8$ rad s⁻¹, edge shear rate of 100 s⁻¹). During the whole measurement, the viscosity was nearly constant and no rheopecty was observed. **g** Frequency sweep of GO-S performed using parallel-plate geometry in oscillatory mode (disc diameter 60 mm and a gap $d = 0.5$ mm). Red line represents the Carreau-Yasuda model fitting using Eq. (2).

($De > De_{crit}$) the elastic instabilities might be expected, similarly to GO-L. Nevertheless, unlike GO-L, the GO-S does not exhibit clear shear bands. Thus, it has to be concluded that $De > De_{crit}$ is a necessary but not a sufficient condition for the formation of elastic instabilities.

To confirm that the observed changes between the two samples were not due to large stability changes, zeta potential (ζ) was measured for both flake sizes: $\zeta_{GO-S} = -60.3$ mV and $\zeta_{GO-L} = -53.6$ mV. The difference in charge repulsions between the flakes of different sizes was minimal and was considered not to play a crucial role in the final structure formation. The exact reason for the difference in GO-L and GO-S viscoelastic behavior is intriguing and should be investigated further, but is out of scope of the current study.

In summary, we have synthesized GO flakes of two lateral size distributions: GO-L: 42.1 ± 29.4 μm and GO-S: 15.5 ± 7.5 μm . Aqueous GO dispersions, especially of large aspect ratio particles, exhibit unique viscoelastic properties and are of significant technological interest. When sheared GO dispersions are observed in Rheo-SIPLI, a combination of polarised light imaging (PLI) with rheological shear experiments, a combined MC and shear-banding pattern in GO-L dispersions was observed. The observed PLI structures appear in the right theoretical regime of elastic flow instabilities, which were supported by calculated GO Deborah numbers exceeding the critical values prescribed in the literature. By considering Taylor vortices as elastic flow instabilities, mathematical modelling revealed that the combination of normal shear flow and Taylor-vortices flow, resulting in alternating bands of twinned left- and right-handed helical flows, explains the obtained unique SIPLI patterns for GO-L. Rheo-SAXS of GO-L using coaxial geometry confirmed the tilted alignment and formation of Taylor-vortices. The observed rheopecty for GO-L flakes at high shear rate also confirmed the elastic instabilities shear alignment theory. Interestingly, a combination of MC and SB was observed to form relatively quickly immediately after imposing shear (<10 s). This demonstrated the high sensitivity of GO-L suspensions to Taylor-like rolls. It is also important to note that this flow is observed under a very wide range of shear rates, which is atypical of all other elastic flow instabilities, making it practically viable for

producing shear-aligned structures for applications such as electrical sensors or soft composites for biomedical applications.

METHODS

GO preparation

GO was prepared following a modified Hummers method described in detail elsewhere⁵⁸. In brief, 10 g of natural graphite (30 mesh size, 95% min) was mixed with 338 ml H₂SO₄ (98%, Sigma Aldrich) and 9 g of NaNO₃ (98%, Alfa Aesar) and left overnight to intercalate. The mixture was then cooled down in an ice bath and 45 g of KMnO₄ (98%, Alfa Aesar) was added slowly under stirring followed by 6 days of oxidation at room temperature. Afterwards, the brown thick slurry was diluted with 1.1 L of H₂SO₄ 5% solution followed by the addition of 30 g of H₂O₂ (30%, Sigma Aldrich) and stirred overnight. The mixture was further diluted with 1 L of solution of H₂SO₄:H₂O₂ (3%:0.5%). The graphite oxide purification and exfoliation were achieved by washing the mixture with 3%:0.5% solution of H₂SO₄:H₂O₂ and DI water at least 15 times with the aid of centrifugation. The resulting GO was homogeneously dispersed with a vertical mixer.

GO flake size reduction

The GO flake size reduction was conducted using a Silverson LSM shear mixer model operating at 9000 rpm for 4 h. During the mixing operation the GO dispersion was kept in an ice bath to prevent it from overheating.

Scanning electron microscopy

The size distribution of all GO dispersions were characterized using scanning electron microscopy (SEM), performed on a Zeiss Ultra FEG SEM. Silicon substrates were cut into 1 cm² pieces, cleaned in acetone, DI water and isopropanol by the aid of sonication and the oven-dried. GO dispersions at 0.5 mg mL⁻¹ were spin coated on to the SiO₂ surface of the silicon substrates, using a spin coater at a speed of 3000 rpm and an acceleration of 300 rpm s⁻¹, to obtain a sub-monolayer coverage with a minimal flake overlap. The sizes of 200 flakes from multiple SEM images for each suspension were measured manually using ImageJ®, always in the horizontal direction through the center of the flake in order that shape anisotropies do not skew the distribution results; it is assumed that the drying process does not introduce any orientation anisotropy.

Atomic force microscopy (AFM)

Samples were prepared identically to the SEM samples. The AFM characterization of the GO was performed using a Bruker Dimension FastScan microscope, operating in tapping mode, with an aluminum-coated silicon tip (FastScan-A, Bruker).

X-ray photoelectron spectroscopy (XPS)

The GO sample was prepared by drop casting on a cleaned the SiO₂ surface of silicon substrates to form a thick film of GO of at least 10 nm (the penetration depth of XPS X-rays is ~10 nm). XPS data were collected on a SPECS custom built system composed of a Phoebos 150 hemispherical electron analyser with 1D detector and a microfocus Al K-alpha X-ray source (energy 1486.6 eV). All spectra were collected with an X-ray source pass energy of 20 eV. The XPS resolution was measured based on Ag 3d peak and was 0.5 eV. The XPS data were processed using CasaXPS software (version 2.3.16 PR 1.6). All spectra were calibrated to 284.8 eV position corresponding to the C-C peak. The C1s region peak was fitted using Gaussian/Lorentzian shape components (for sp³ carbon) and asymmetric shape components (for sp² carbon) respectively. XPS C1s region was fitted with the synthetic components in the manner, which minimizes the total square error fit and corresponds to the literature reports.

Raman spectroscopy

The samples were prepared using the same procedure as for the XPS measurements. Raman spectra were obtained on a Renishaw Raman imaging microscope (inVia) equipped with a Leica microscope and a CCD detector. Raman spectra were recorded using 532 nm laser line (Cobolt Samba™ continuous wave diode-pumped solid-state laser, 20 mW), and the laser power was kept below 10 μW to avoid thermal degradation of the samples. Raman spectra were acquired as a line mapping (two mappings for each sample, 20 points, 1 s integration time, two accumulations). The spectra were processed in Wire software (version 4.1).

Zeta potential (ζ) measurements

The charge of the GO dispersions was measured at a concentration of 0.02 mg mL⁻¹ using Malvern Zetasizer ESA9800. The measurements were performed at room temperature 21 °C (RT). The values presented are an average of three replicates.

Rheometer-coupled SIPLI

Rheo-SIPLI measurements were performed using a setup described in detail elsewhere²⁷. In brief, the PLI device (RheoOptics-Polarized Imaging, Anton Paar, Graz, Austria) was attached to a rotational stress-controlled rheometer (Physica MCR 301, Anton Paar) (Fig. 1a). It consists of a parallel-plate rheometer with a bottom transparent plate and a top reflective plate (polished steel mirror), allowing reflected PLIs to be recorded during shear²⁷. In the Rheo-SIPLI configuration used here (Fig. 1a), initially, the light passes through a polarizer and becomes linearly polarized. It then passes through a beam splitter (not shown) and a transparent bottom glass plate, interacts with the sample and is incident on the top reflective plate. The reflected light propagates through the sample for the second time, passes through the bottom transparent plate, the beam splitter, a linear analyzer crossed at 90 degrees in respect to the polarizer plane and is finally incident on a CCD camera (detector). In this manner, PLI can be performed on samples, prior to, during, and after the application of shear forces. In this case, the optical path the polarized light traverses is as follows: polariser (P) → beam splitter → sample → top mirror plate → sample → beam splitter → analyser (A) → detector. The SIPLI setup can be equipped with QWPs in order to record PLIs using circularly polarized light. This changes the path of the polarized light, which goes as follows: P → QWP → beam splitter → transparent bottom plate → sample → top mirror plate → sample → transparent bottom plate → beam splitter → QWP → A → detector. Each of the GO samples was firstly placed on the rheometer using positive displacement pipette. The PLIs were then taken using a polarizer and an analyzer with their polarization planes oriented at 90° to each other (cross-polarized) in order to monitor birefringence of the sample. In another setup a circularly polarized light was used for the imaging: a QWP was used together with a linear polarizer. The samples were sheared for 120 s at a constant angular speed ($\omega = 0.08 \text{ rad s}^{-1}$, $\omega = 0.8 \text{ rad s}^{-1}$ or $\omega = 8.0 \text{ rad s}^{-1}$) using parallel-plate geometry (Fig. 1a) with the gap thickness between the two plates $d = 1 \text{ mm}$. The PLIs for all setups were recorded at a rate five images s⁻¹ for 140 s followed by another 60 s

with a recording rate of 0.2 images s⁻¹ (a relaxation phase of the experiment). All the measurements were performed at RT.

In the most general consideration, the flakes (or platelets) of a sheared suspension, can align in three possible orientations or combinations thereof^{54,59} (Fig. 1c): transverse, with the flake normal parallel to the flow direction, x ; perpendicular, with the flake normal parallel to the vorticity direction, y ; parallel, with the flake normal parallel to the shear gradient direction, z . If the axis of the birefringence ellipsoid of an optically uniaxial material is oriented perpendicular to the platelet normal then under crossed polarizer and analyser, both transverse and perpendicular alignment can produce a MC and parallel alignment produces a dark image (complete extinction) as the material is non-birefringent in the x - y plane.

In Rheo-SIPLI light transmission is blocked in regions where the flakes are oriented parallel to either the polarizer or analyzer plane, and transmitted through the regions where the flakes are at an intermediate angle between the polarizer and analyzer planes. This pattern comprised of bright and dark regions is typically known as an MC. Such a pattern is commonly observed under crossed polarizers for birefringent materials in which one of the principal axes of the optical birefringence ellipsoid is always parallel to the radial direction originating from the MC center, for example in polymer spherulites (in which polymer crystals grow radially from the nucleation center)⁶⁰.

In torsional parallel-plate geometry, the shear rate across the sample increases radially from the center of an image (0 s^{-1}) to a maximum at the outer edge of the plate according to the following linear relationship:

$$\dot{\gamma} = \frac{\omega r}{d} \quad (4)$$

where r is radial distance from the center of rotation of the shearing disc plate. With given angular speeds (0.08, 0.8, and 8 rad s⁻¹) and a sample gap $d = 1 \text{ mm}$, the calculated sample edge shear rates are $\dot{\gamma} = 1 \text{ s}^{-1}$, $\dot{\gamma} = 10 \text{ s}^{-1}$, and $\dot{\gamma} = 100 \text{ s}^{-1}$, respectively (Fig. 1d–l).

Rheometer-coupled SAXS

Rheo-SAXS experiments were performed on beamline I22 at the Diamond Light Source synchrotron (DLS, Didcot, UK). The Rheo-SAXS arrangement comprises of two concentric cylinders, a fixed outer cylinder and a rotating inner cylinder providing the two shear surfaces between which fluid is confined. The energy of the beam was 12.4 keV corresponding to the X-ray wavelength of 0.1 nm. Acquisition time was set at 20 s and the Pilatus P3-2M area hybrid pixel detector (Dectris, Switzerland) used to collect SAXS data. The distance between samples and the detector was fixed to 3.73 m, resulting in a scattering vector modulus range of $0.03 \text{ nm}^{-1} < q < 3.6 \text{ nm}^{-1}$ with $q = (4\pi/\lambda)\sin(\theta)$, where 2θ is the scattering angle and λ is the wavelength of incident X-ray photons. Lateral calibration of the scattering patterns was performed using silver behenate powder. 2D SAXS data were reduced to 1D scattering curves using a Dawn software package. A rotational stress-controlled rheometer (Physica MCR 501, Anton Paar) equipped with a concentric cylinder shear cell (the cell is made of polished polycarbonate, rotating inner cylinder of radius 24 mm and the sample gap $d = 1 \text{ mm}$) was mounted on the beamline placed in the beam direction and radial and tangential spots were measured. All the measurements were carried out at RT.

Oscillatory rheology

Oscillatory rheology was performed on a rotational stress-controlled rheometer (Haake RS6000, Thermo Scientific, Karlsruhe, Germany), using parallel-plate geometry (disc diameter 60 mm and the sample gap $d = 0.5 \text{ mm}$). Each sample was carefully poured down directly onto a bottom rheometer plate from the glass vial, preliminary stored for at least 1 day in a fridge at 4 °C, and left for at least 10 min to equilibrate and relax. A solvent trap was used to prevent water evaporation from the samples. Two strategies were chosen for the rheological measurements: amplitude sweeps performed on the samples at frequency $f = 0.1 \text{ Hz}$ and frequency sweeps performed at strain values of $\gamma = 0.1\%$. All the measurements were carried out at RT.

DATA AVAILABILITY

Correspondence and requests for materials should be addressed to A.V. The data obtained in this study are available on reasonable request from corresponding author.

Received: 27 September 2020; Accepted: 5 December 2020;

Published online: 08 January 2021

REFERENCES

- Stankovich, S. et al. Graphene-based composite materials. *Nature* **442**, 282–286 (2006).
- Zongping, C. et al. Three-dimensional flexible and conductive interconnected graphene networks grown by chemical vapour deposition. *Nat. Mater.* **10**, 424–428 (2011).
- Ramanathan, T. et al. Functionalized graphene sheets for polymer nanocomposites. *Nat. Nanotechnol.* **3**, 327–331 (2008).
- Frank, S. Graphene transistors. *Nat. Nanotechnol.* **5**, 487 (2010).
- Goki, E., Giovanni, F. & Manish, C. Large-area ultrathin films of reduced graphene oxide as a transparent and flexible electronic material. *Nat. Nanotechnol.* **3**, 270–274 (2008).
- Abraham, J. et al. Tuneable sieving of ions using graphene oxide membranes. *Nat. Nanotechnol.* **12**, 546–550 (2017).
- Kian Ping, L., Qiaoliang, B., Goki, E. & Manish, C. Graphene oxide as a chemically tunable platform for optical applications. *Nat. Chem.* **2**, 1015–1024 (2010).
- Yoon, H. J. et al. Sensitive capture of circulating tumour cells by functionalized graphene oxide nanosheets. *Nat. Nanotechnol.* **8**, 735–741 (2013).
- Jalili, R. et al. Formation and processability of liquid crystalline dispersions of graphene oxide. *Mater. Horiz.* **1**, 87–91 (2014).
- Yang, X. M., Guo, C. X., Ji, L. L., Li, Y. W. & Tu, Y. F. Liquid crystalline and shear-induced properties of an aqueous solution of graphene oxide sheets. *Langmuir* **29**, 8103–8107 (2013).
- Yao, B. W., Chen, J., Huang, L., Zhou, Q. Q. & Shi, G. Q. Base-induced liquid crystals of graphene oxide for preparing elastic graphene foams with long-range ordered microstructures. *Adv. Mater.* **28**, 1623–1629 (2016).
- Xu, Z. & Gao, C. Aqueous liquid crystals of graphene oxide. *ACS Nano* **5**, 2908–2915 (2011).
- Xu, Z. & Gao, C. Graphene chiral liquid crystals and macroscopic assembled fibres. *Nat. Commun.* **2**, 571 (2011).
- Narayan, R., Kim, J. E., Kim, J. Y., Lee, K. E. & Kim, S. O. Graphene oxide liquid crystals: discovery, evolution and applications. *Adv. Mater.* **28**, 3045–3068 (2016).
- Kim, J. E. et al. Graphene oxide liquid crystals. *Angew. Chem. Int. Ed.* **50**, 3043–3047 (2011).
- Dan, B. et al. Liquid crystals of aqueous, giant graphene oxide flakes. *Soft Matter* **7**, 11154–11159 (2011).
- Chowdhury, I., Duch, M. C., Mansukhani, N. D., Hersam, M. C. & Bouchard, D. Colloidal properties and stability of graphene oxide nanomaterials in the aquatic. *Environ. Sci. Technol.* **47**, 6288–6296 (2013).
- Poulin, P. et al. Superflexibility of graphene oxide. *PNAS* **113**, 11088–11093 (2016).
- Akbari, A. et al. Large-area graphene-based nanofiltration membranes by shear alignment of discotic nematic liquid crystals of graphene oxide. *Nat. Commun.* **7**, 10891 (2016).
- Al-Zangana, S., Iliut, M., Turner, M., Vijayaraghavan, A. & Dierking, I. Confinement effects on lyotropic nematic liquid crystal phases of graphene oxide dispersions. *2D Mater.* **4**, 041004 (2017).
- Kim, I. H. et al. Mussel-Inspired Defect Engineering of Graphene Liquid Crystalline Fibers for Synergistic Enhancement of Mechanical Strength and Electrical Conductivity. *Adv. Mater.* **30**, 1803267 (2018).
- Jiang, Y., Guo, F., Xu, Z., Gao, W. & Gao, C. Artificial colloidal liquid metacrystals by shearing microlithography. *Nat. Commun.* **10**, 4111 (2019).
- Cinader, D. K. & Burghardt, W. R. Mixed orientation state induced by expansion flow of a thermotropic liquid-crystalline polymer. *Macromolecules* **31**, 9099–9102 (1998).
- Hongladarom, K. et al. Birefringence, X-ray scattering, and neutron scattering measurements of molecular orientation in sheared liquid crystal polymer solutions. *Macromolecules* **29**, 5346–5355 (1996).
- Helfrich, W. Molecular theory of flow alignment of nematic liquid crystals. *J. Chem. Phys.* **50**, 100 (1969).
- Hongladarom, K. & Burghardt, W. R. Molecular alignment of polymer liquid-crystals in shear flows. 2. Transient flow behavior in poly(benzyl glutamate) solutions. *Macromolecules* **26**, 785–794 (1993).
- Mykhaylyk, O. O., Warren, N. J., Parnell, A. J., Pfeifer, G. & Laeuger, J. Applications of shear-induced polarized light imaging (SIPLI) technique for mechano-optical rheology of polymers and soft matter materials. *J. Polym. Sci. Pol. Phys.* **54**, 2151–2170 (2016).
- Ma, L. L. et al. Rationally designed dynamic superstructures enabled by photo-aligning cholesteric liquid crystals. *Adv. Opt. Mater.* **3**, 1691–1696 (2015).
- Fardin, M. A. et al. Taylor-like Vortices in Shear-Banding Flow of Giant Micelles. *Phys. Rev. Lett.* **103**, 028302 (2009).
- Shaqfeh, E. S. G. Purely elastic instabilities in viscometric flows. *Annu. Rev. Fluid Mech.* **28**, 129–185 (1996).
- Byars, J. A., Oztekin, A., Brown, R. A. & McKinley, G. H. elastic fluids between rotating parallel disks. *J. Fluid Mech.* **271**, 173–218 (1994).
- Archer, L. A. & Larson, R. G. A molecular theory of flow-alignment and tumbling in sheared nematic liquid-crystals. *J. Chem. Phys.* **103**, 3108–3111 (1995).
- He, P. & Derby, B. Inkjet printing ultra-large graphene oxide flakes. *2D Mater.* **4**, 021021 (2017).
- McManus, D. et al. Water-based and biocompatible 2D crystal inks for all-inkjet-printed heterostructures. *Nat. Nanotechnol.* **12**, 343–350 (2017).
- Xin, G. et al. Microfluidics-enabled orientation and microstructure control of macroscopic graphene fibres. *Nat. Nanotechnol.* **14**, 168–175 (2019).
- Naficy, S. et al. Graphene oxide dispersions: tuning rheology to enable fabrication. *Mater. Horiz.* **1**, 326–331 (2014).
- Mykhaylyk, O. O. Time-resolved polarized light imaging of sheared materials: application to polymer crystallization. *Soft Matter* **6**, 4430–4440 (2010).
- Mykhaylyk, O. O., Parnell, A. J., Pryke, A. & Fairclough, J. P. A. Direct imaging of the orientational dynamics of block copolymer lamellar phase subjected to shear flow. *Macromolecules* **45**, 5260–5272 (2012).
- Hong, S. H., Shen, T. Z. & Song, J. K. Flow-induced alignment of disk-like graphene oxide particles in isotropic and biphasic colloids. *Mol. Cryst. Liq. Cryst.* **610**, 68–76 (2015).
- Kumar, P., Maiti, U. N., Lee, K. E. & Kim, S. O. Rheological properties of graphene oxide liquid crystal. *Carbon* **80**, 453–461 (2014).
- Onsager, L. The effects of shape on the interaction of colloidal particles. *Ann. NY Acad. Sci.* **51**, 627–659 (1949).
- Wang, H.-F. et al. Handedness of twisted lamella in banded spherulite of chiral poly(lactides) and their blends. *Macromolecules* **50**, 5466–5475 (2017).
- Vasu, K. S., Krishnaswamy, R., Sampath, S. & Sood, A. K. Yield stress, thixotropy and shear banding in a dilute aqueous suspension of few layer graphene oxide platelets. *Soft Matter* **9**, 5874–5882 (2013).
- Brown, A. B. D. & Rennie, A. R. Images of shear-induced phase separation in a dispersion of hard nanoscale discs. *Chem. Eng. Sci.* **56**, 2999–3004 (2001).
- Lin-Gibson, S., Pathak, J. A., Grulke, E. A., Wang, H. & Hobbie, E. K. Elastic flow instability in nanotube suspensions. *Liq. Cryst.* **92**, 048302 (2004).
- Kang, K. G., Lettinga, M. P., Dogic, Z. & Dhont, J. K. G. Vorticity banding in rodlike virus suspensions. *Phys. Rev. E* **74**, 026307 (2006).
- Hong, S. H., Shen, T. Z. & Song, J. K. Shear-induced assembly of graphene oxide particles into stripes near surface. *Liq. Cryst.* **45**, 1303–1311 (2018).
- Frocht, M. M. & Mayer, W. G. Photoelasticity. *Phys. Today* **17**, 58–58 (1964).
- Macosko, C. W. *Rheology: principles, measurements, and applications*. (Wiley, 1994).
- Goswami, J. & Davis, V. K. Viscoelasticity of single-walled carbon nanotubes in unsaturated polyester resin: effects of purity and chirality distribution. *Macromolecules* **48**, 8641–8650 (2015).
- Phanthien, N. Cone-and-plate flow of the Oldroyd-B fluid is unstable. *J. Non-Newton. Fluid* **17**, 37–44 (1985).
- Phanthien, N. Coaxial-disk flow of an Oldroyd-B fluid – exact solution and stability. *J. Non-Newton. Fluid* **13**, 325–340 (1983).
- Jin, H., Kang, K., Ahn, K. H. & Dhont, J. K. G. Flow instability due to coupling of shear-gradients with concentration: non-uniform flow of (hard-sphere) glasses. *Soft Matter* **10**, 9470 (2014).
- Krishnamoorti, R. & Yurekli, K. Rheology of polymer layered silicate nanocomposites. *Curr. Opin. Colloid.* **6**, 464–470 (2001).
- Burghardt, W. R., Ugaz, V. M. & Cinader, D. K. in *Scattering from Polymers* Vol. 739 *ACS Symposium Series* Ch. **24**, 374–389 (American Chemical Society, 1999).
- Lettinga, M. P. et al. Nonlinear behavior of nematic platelet dispersions in shear flow. *Phys. Rev. Lett.* **109**, 246001–246005 (2012).
- Kaupp, G. Mechanochemistry: the varied applications of mechanical bond-breaking. *Crystengcomm* **11**, 388–403 (2009).
- Rourke, J. P. et al. The real graphene oxide revealed: stripping the oxidative debris from the graphene-like sheets. *Angew. Chem. Int. Ed.* **50**, 3173–3177 (2011).
- Lin-Gibson, S., Kim, H., Schmidt, G., Han, C. C. & Hobbie, E. K. Shear-induced structure in polymer-clay nanocomposite solutions. *J. Colloid Interf. Sci.* **274**, 515–525 (2004).
- Stein, R. S. & Powers, J. *Topics in Polymer Physics*. (Imperial College Press, 2006).

ACKNOWLEDGEMENTS

We are grateful to Diamond Light Source for beam time awards (SM15478, SM14948, and SM12950) to this project and to the staff on beamline I22 for their support with the Rheo-SAXS experiments. We acknowledge financial support of the Engineering and Physical Sciences Research Council (EPSRC) for Northwest Nanoscience Doctoral Training Center (NOWNANO DTC) (EP/G03737X/1) grant, and EPSRC doctoral training award (DTA) from the Department of Materials, The University of Manchester.

AUTHOR CONTRIBUTIONS

J.K.W., O.O.M., S.E., and A.V. conceived and designed the experiments. M.I. synthesized and characterized the GO samples. J.K.W. performed the scattering and the shear rheology-based experiments. S.E. and J.K.W. developed the mathematical model. B.B. performed oscillatory rheology experiments and contributed to Carreau-Yasuda data analysis and interpretation. C.M. performed XPS measurements. O.O.M. contributed to the SIPLI measurements and SAXS interpretation. J.K.W., O.O.M., S.E., and A.V. analyzed the data and co-wrote the paper. All authors commented on the paper.

COMPETING INTERESTS

The authors declare no competing interests.

ADDITIONAL INFORMATION

Supplementary information is available for this paper at <https://doi.org/10.1038/s41699-020-00193-x>.

Correspondence and requests for materials should be addressed to A.V.

Reprints and permission information is available at <http://www.nature.com/reprints>

Publisher's note Springer Nature remains neutral with regard to jurisdictional claims in published maps and institutional affiliations.



Open Access This article is licensed under a Creative Commons Attribution 4.0 International License, which permits use, sharing, adaptation, distribution and reproduction in any medium or format, as long as you give appropriate credit to the original author(s) and the source, provide a link to the Creative Commons license, and indicate if changes were made. The images or other third party material in this article are included in the article's Creative Commons license, unless indicated otherwise in a credit line to the material. If material is not included in the article's Creative Commons license and your intended use is not permitted by statutory regulation or exceeds the permitted use, you will need to obtain permission directly from the copyright holder. To view a copy of this license, visit <http://creativecommons.org/licenses/by/4.0/>.

© The Author(s) 2021